Published on 26 May 2015. Downloaded by Korea Institute of Science and Technology / KIST on 16/06/2015 03:42:25.

CrystEngComm

PAPER

View Article Online
View Journal

Cite this: DOI: 10.1039/c5ce00752f

Synthesis and characterization of single-crystal Cu(In,Ga)Se_2 nanowires: high Ga contents and growth behaviour†

J. Y. Lee,‡[ab] W. K. Seong,‡§[a] J.-H. Kim,[a] S.-H. Cho,[a] J.-K. Park,[a] K.-R. Lee,[a] M.-W. Moon*[a] and C.-W. Yang*[c]

Received 17th April 2015,
Accepted 25th May 2015

DOI: 10.1039/c5ce00752f

www.rsc.org/crystengcomm

Precise control over the defect density, a high Ga content, and uniform stoichiometry are critical for controlling the physical and optical properties of Cu(In,Ga)Se_2 (CIGS) nanowires (NWs). In this study, we investigated the synthesis of epitaxially grown, single-crystal CIGS NWs by a vapour-phase transport method using multiple sources of Ga_2Se_3, In_2Se_3, and Cu_2Se as the precursors. No catalysts were employed, and *r*-cut Al_2O_3 substrates were used for the fabrication of the NWs. The synthesized CIGS NWs had a uniform composition along their length, and the NWs with the highest Ga/(In + Ga) content ratio (0.8) had a chalcopyrite structure. The bandgap energy of the CIGS NWs was higher than that of typical CIGS thin films grown by co-evaporation methods because of the high Ga content ratio. These single-crystal CIGS NWs offer an attractive platform for exploring various concepts related to hierarchical nanostructures and devices based on fully epitaxial semiconductor structures.

Introduction

The I–III–VI_2 family of semiconducting compounds, which includes $CuIn_{1-x}Ga_xSe_2$ (CIGS), has been widely used in photovoltaics because of its many advantages. For example, CIGS exhibits a direct bandgap, high absorption coefficients for visible light with wavelengths of up to approximately 10^5 cm^{-1}, and long-term optoelectronic stability.[1–4] In addition, the bandgap energy of CIGS can be tuned by varying the compositional ratio, Ga/(In + Ga). The direct bandgap energy can be tuned from around 1.03 eV in the case of $CuInSe_2$ (CIS) to approximately 2.5 eV in the case of $CuGaS_2$.[5] The performance of CIS and CIGS-based photovoltaics can be further improved by exploiting their nanostructures, which are unique. They have a tuneable bandgap, large specific surface area, well-defined conducting pathways, and exhibit carrier multiplication.[6] Recently, significant efforts have been devoted to the fabrication of various CIS and CIGS nanostructures, including nanocrystals, nanorods, and nanowires (NWs), with a variety of methods.[7–10] CIGS nanocrystals can be synthesized using a low-cost solution-based method, which allows the production of large-scale arrays.[7,11] However, to enhance their efficiency, the fabrication of nanocrystals with a high Ga content ratio is difficult because the standard electrochemical potential of Ga is much lower than that of the other constituent elements. In addition, CIGS NWs grown using the template method using an anodic alumina membrane (AAM) exhibit poor crystallinity.[8,12] Therefore, precise control over the defect density, a high Ga content ratio, and uniform stoichiometry are essential for producing CIGS NWs that are suitable for photovoltaic applications. These criteria may be achieved by using the vapour-phase transport method as the fabrication technique, which has a few advantages over the solution-based chemical methods. First, the vapour-phase transport method does not require a catalyst or seed layer because the NWs can be grown directly from the substrate. Second, the morphology and size of the synthesized NWs can be readily controlled by adjusting the main synthesis parameters, such as the local temperature, gas deposition flux, and reaction time. However, CIGS NWs have not yet been synthesized using the vapour-phase transport method because of the difficulty in synthesizing NWs from quaternary compounds, as well as the large differences in the vapour pressures of the constituent elements.

[a] *Institute for Multi-Disciplinary Convergence of Matter, Korea Institute of Science and Technology (KIST), Seoul 130–650, Republic of Korea. E-mail: mwmoon@kist.re.kr; Fax: +82 2 958 5509; Tel: +82 2 958 5487*

[b] *Advanced Analysis Center, Korea Institute of Science and Technology (KIST), Seoul 130–650, Republic of Korea*

[c] *School of Advanced Materials Science and Engineering, Sungkyunkwan University, Suwon 440–746, Republic of Korea. E-mail: cwyang@skku.edu; Fax: +82 31 290 7410; Tel: +82 31 290 7362*

† Electronic supplementary information (ESI) available: Experimental setup (Fig. S1), SEM micrographs of the freestanding and horizontally grown CIGS NWs (Fig. S2), STEM-EDS analysis of a freestanding CIGS NW (Fig. S3), cross-sectional TEM micrographs and SAED analysis of a horizontally grown CIGS NW in the radial direction (Fig. S4), and the orientation relationship between the CIGS NWs and Al_2O_3 substrate (Fig. S5). See DOI: 10.1039/c5ce00752f

‡ Ji Yeong Lee and Won Kyung Seong contributed equally to this work.

§ Present address: Quantum Design Korea, #303 Dongshin bldg., 204, Dogok-ro, Kangnam-gu, Seoul, Korea.

Published on 26 May 2015. Downloaded by Korea Institute of Science and Technology / KIST on 16/06/2015 03:42:25.

Herein, we report the epitaxial growth of single-crystal CIGS NWs with high Ga contents *via* the vapour-phase transport method using multiple precursors. The CIGS NWs grown had an epitaxial relationship with the *r*-cut Al_2O_3 substrates used, which showed a 1.5% lattice mismatch. The CIGS NWs had high crystallinity, with {112} facets and a (110) growth direction. They also had a Ga-rich CIGS stoichiometry and bandgap energy of 1.12 eV. During the growth process, we observed two types of CIGS NWs, *i.e.*, freestanding and horizontal NWs, on the *r*-cut Al_2O_3 substrates depending on the gas deposition flux. It is well-known that the growth behaviour of NWs can be controlled by varying the gas deposition flux.[13] We employed a specially designed alumina boat with an alumina cap to achieve a high deposition flux around the substrate.[14] A detailed schematic of the chemical vapour deposition (CVD) process is shown in Fig. S1 in the ESI.† We were able to fabricate the CIGS NWs with high Ga contents by using multiple alloy-based precursors to control the mobility of the constituent elements in the absence of catalysts.

Experimental methods

Synthesis of CIGS NWs

The single-crystal CIGS NWs were grown on Al_2O_3 substrates in a horizontal tube furnace equipped with a 3-inch-diameter quartz tube. After placing the alumina boat containing the substrate and the In_2Se_3 (Alfa Aesar, 99.99%), Cu_2Se (Alfa Aesar, 99.5%) and Ga_2Se_3 (Alfa Aesar, 99.99%) powders in the reactor, we purged the reactor several times with a mixture of high-purity H_2 and N_2 gases. The alumina boat was then heated to either 900 °C for freestanding growth or 950 °C for horizontal growth under a reactor pressure of 5 Torr in an ambient gas mixture. The total flow rate of the gas mixture was 100 sccm. Additional quantities of In_2Se_3, Ga_2Se_3, and CuI powders (Alfa Aesar, 98%) were placed in a low-temperature region of the furnace to adjust the concentrations of Cu, In, and Ga in the CIGS NWs. Once the growth process was complete, the samples were allowed to cool naturally to room temperature in an ambient gas mixture.

Characterization

The macrostructure of the synthesized CIGS nanostructures was investigated by X-ray diffraction (XRD, Dmax 2500, Rigaku), which was performed using Cu Kα X-rays. To determine the chemical composition, growth direction, and crystal structure of the CIGS NWs, transmission electron microscopy (TEM, FEI Tecnai G2) was employed. The microstructure and chemical composition of the CIGS NWs were also analysed by high-resolution TEM (HR-TEM, which was performed at 200 kV in combination with scanning transmission electron microscopy (STEM) and energy dispersive X-ray spectroscopy (EDS). Selected-area electron diffraction (SAED) patterns of the CIGS NWs were obtained to determine their crystallographic phases; the cross-sectional CIGS NW specimens were prepared by the lift-out technique using focused ion beam (FIB) milling. Pt and a commercial epoxy were used to protect the surface of the CIGS NWs by preventing both the re-deposition of the removed materials and damage to the NWs from the ion beam during the sample preparation.

The horizontal CIGS NWs grown on an *r*-cut Al_2O_3 substrate were used for the micro-Raman spectroscopy and photoluminescence (PL) measurements. The micro-Raman spectroscopy measurements (alpha 300 R, WITec) were performed using an Nd:YAG laser with a wavelength of 532 nm and a laser power of 15 mW at room temperature. The alpha 300 R system combines a confocal microscope of extremely high optical throughput and resolution with a sensitive Raman spectrometer. This instrument is not only able to collect Raman spectra, but it is also able to take high-resolution Raman images. The images obtained show the integral intensities of the Raman modes. PL is widely used to study the bandgap energy and structural defects of semiconductor materials. The PL spectra of CIGS-based materials are very sensitive to point defects and deviations from the ideal stoichiometry. The low-temperature PL spectra of the CIGS NWs were used to measure the bandgap energy of the NWs at an average temperature of 10 K. The samples were excited using a diode-pumped solid-state (DPSS) continuous-wave laser with a wavelength of 532 nm (SDL-532-300 T, Dreamlaser) at a pump power of 130 mW. The emission from the samples was collected with collimation lenses and then dispersed using a monochromator (SpectraPro 2300i, Princeton (Acton)) with a focal length of 300 mm and a spectral resolution of 0.1 nm. The dispersed optical signals were detected with a thermoelectrically (TE) cooled InGaAs photodetector (one-stage TE-cooled type, Hamamatsu) and amplified using a lock-in amplifier.

Results and discussion

For the synthesis of quaternary I–III–VI_2 nanostructures, the balancing of each elemental source's reactivity needs to be considered to form NWs with a homogeneous stoichiometry. Therefore, metal selenides were used as the precursors to fabricate various CIGS nanostructures. The CIGS nanostructures were synthesized using a vapour-phase transport method by controlling the local temperature, gas deposition flux, and reaction time. The schematic diagram of the thermal CVD process is shown in Fig. S1.† We then investigated the epitaxial relationship between the individual planes of the Al_2O_3 substrate and CIGS nanostructures. The morphology of the CIGS nanostructures grown on the *a*, *c*, and *r*-cut Al_2O_3 substrates under similar conditions was investigated with a field-emission scanning electron microscopy (FE-SEM, Nova 600, FEI) setup equipped with a dual-beam focused ion beam (FIB) system; the FE-SEM results are shown in Fig. 1(a–c).

As can be seen in the insets in Fig. 1(a) and (b), the CIGS nanostructures grown on the *a* and *c*-cut Al_2O_3 substrates have truncated triangular and hexagonal plate morphologies, respectively. The average sizes of the truncated triangular and hexagonal CIGS nanostructures are approximately 1.1 μm and 1.5 μm, respectively. As the growth time increased,

 This journal is © The Royal Society of Chemistry 2015

Published on 26 May 2015. Downloaded by Korea Institute of Science and Technology / KIST on 16/06/2015 03:42:25.

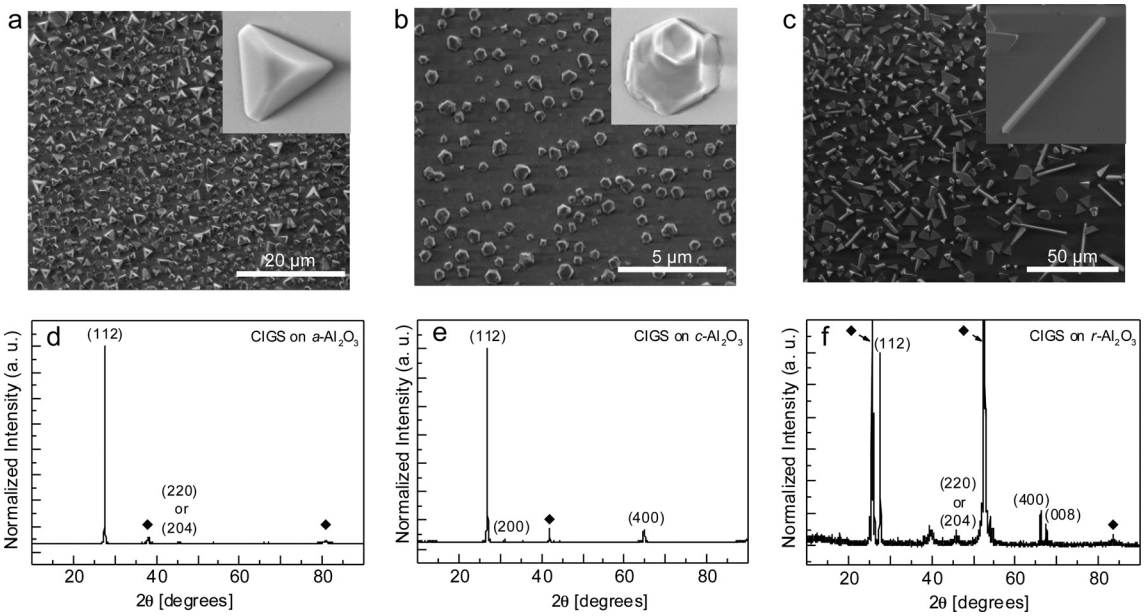

Fig. 1 The FE-SEM micrographs of the CIGS nanostructures grown on the (a) *a*, (b) *c*, and (c) *r*-cut Al_2O_3 substrates. The insets show the high-magnification images of the individual CIGS nanostructures. The XRD patterns of the CIGS nanostructures on the (d) *a*, (e) *c*, and (f) *r*-cut Al_2O_3 substrates were obtained to determine the differences between the crystalline structures of the substrates. The "◆" symbols denote the peaks of the substrates: the $(11\bar{2}0)$ plane in (d), the (0006) plane in (e), and the $(01\bar{1}2)$, $(02\bar{2}4)$, $(03\bar{3}6)$ planes in (f).

the truncated triangular and hexagonal plates became larger, but NWs were not formed. The CIGS NWs only grew on the *r*-cut Al_2O_3 substrate because of the orientation relation between the CIGS NWs and the substrate, as shown in Fig. 1(c). This epitaxial relationship between the CIGS NWs and the *r*-cut Al_2O_3 substrate is described in more detail in Fig. 3. To confirm the differences between the individual planes of the Al_2O_3 substrates, we performed XRD measurements.

The XRD patterns are shown in Fig. 1(d–f). The substrate peaks are marked with the "◆" symbol. The XRD peaks were indexed with the JCPDS file (#35-1101) for CIGS. The cell parameters of the CIGS NWs are a = 0.568 nm and c = 1.126 nm, and they have a $I\bar{4}2d$ space group, as well as a tetragonal structure. The XRD patterns indicate the presence of single-crystal CIGS without any impurities or changes in the crystal structure. As can be seen in Fig. 1(d–f), the (112) plane of CIGS is very intense in all of the XRD patterns, which has a *d*-spacing of 0.32 nm ± 0.003 nm. According to recent studies, the polar (112) surface of CIGS is considerably more stable than the non-polar (110) surface.[15] Thus, CIGS-based materials exhibit the spontaneous formation of micro-facets with polar surfaces when one attempts to grow them on a non-polar chalcopyrite surface.[15] The changes in the relative intensities of the XRD peaks, except for the (112) plane, are dependent on the changes in morphology, *e.g.*, from truncated triangles to truncated hexagons to NWs.

As shown in Fig. S2(a) and (b),† the growth direction of the NWs can be controlled by adjusting the gas deposition flux on the *r*-cut Al_2O_3 substrate. The freestanding NWs were grown at 900 °C in the normal alumina boat without the cap. The high-deposition flux at 950 °C, which was achieved by using a specially designed alumina boat, led to the horizontal growth of CIGS NWs and increased their size. Under the low-deposition flux, the diameters and lengths of the freestanding CIGS NWs are approximately 50–700 nm and 1–20 μm, respectively, while that of the horizontally grown CIGS NWs on the *r*-cut Al_2O_3 substrate are approximately 500–1500 nm and 1–100 μm, respectively.

To determine the chemical composition and crystal structure of the CIGS NWs, we performed STEM/EDS and HR-TEM/SAED measurements. Fig. 2(a) shows a cross-sectional TEM micrograph of a horizontally grown CIGS NW with a diameter of 900 nm and a length of 15 μm, which was prepared by the lift-out technique of FIB milling. We recorded the STEM/EDS spectrum and elemental mapping of the CIGS NW, which are displayed in Fig. 2(b) and (c), respectively, with the mapping results clearly showing the spatial distribution of Cu (orange), In (yellow), Ga (green), and Se (red). The average contents were estimated to be 23.4 at.% Cu, 4.8 at.% In, 21.1 at.% Ga, and 50.5 at.% Se, as shown in Fig. 2(d).

Therefore, the Cu/(In + Ga) and Ga/(In + Ga) ratios of the horizontally grown CIGS NWs are 0.9 and 0.81, respectively. In addition, each element in the CIGS NW is uniformly distributed along the growth direction. The chemical composition of the freestanding CIGS NW is also uniformly distributed along the growth direction, but with a Ga-rich phase, as shown in Fig. S3.† A number of researchers have tried to increase the Ga content in CIGS to obtain higher cell efficiencies in photovoltaic systems because the bandgap of CIGS increases linearly with an increase in its Ga content.[7] However, until now, the concentrations of the different

Published on 26 May 2015. Downloaded by Korea Institute of Science and Technology / KIST on 16/06/2015 03:42:25.

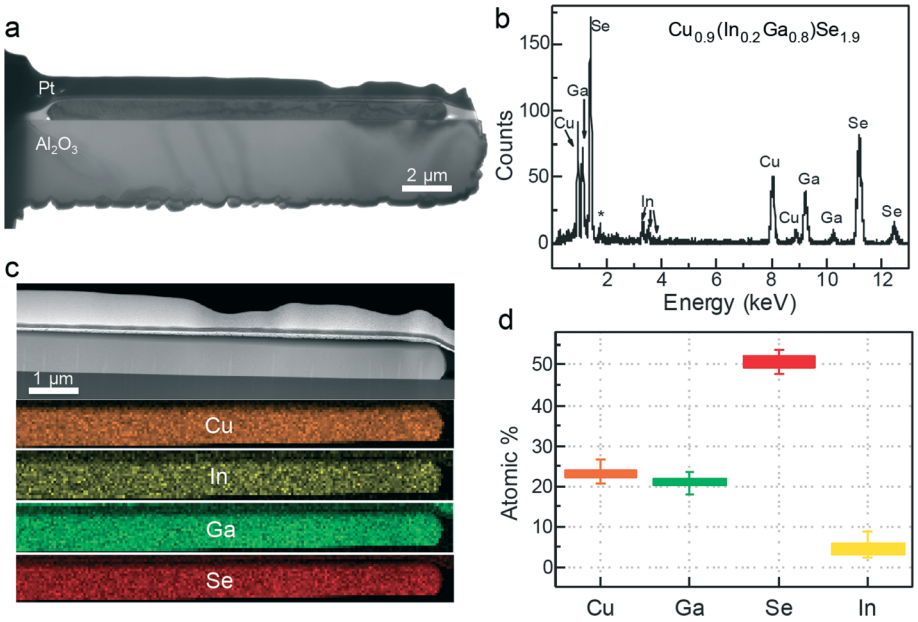

Fig. 2 (a) The cross-sectional TEM micrograph of a horizontal CIGS NW on an *r*-cut Al_2O_3 substrate. Pt and a polymer were used to protect the surface of the NW during the sample preparation. (b) A typical STEM/EDS spectrum of a horizontal CIGS NW. The "*" symbol denotes the detector peak. (c) The STEM image of the CIGS NW (top image). The elemental maps of Cu, In, Ga, and Se (bottom images) were obtained by STEM/EDS. (d) A graph showing the average elemental concentrations along the length of a horizontal CIGS NW.

constituent elements in CIGS thin films and nanostructures could not be controlled successfully because of the differences between the vapour pressures of the elements and their environmental sensitivities during the evaporation process. In spite of the many difficulties, the synthesis of the Ga-rich CIGS phases is quite important for various applications. Therefore, in this study, we have successfully synthesized CIGS NWs with high Ga contents by using multiple precursors without any catalysts.

To investigate the growth direction and crystal structure of the CIGS NWs in detail, HR-TEM and SAED measurements were conducted on a CIGS NW that was placed on a carbon supporting film with several zone axes parallel to the electron beam, as shown in Fig. 3(a–d). In Fig. 3(a), the spacing of the lattice planes parallel and perpendicular to the long axis of the NW are 0.205 nm and 0.322 nm, which are consistent with the $(1\bar{1}0)$ and (112) planes of the CIGS chalcopyrite structure, respectively. The corresponding SAED pattern (the inset in Fig. 3(a)) is indexed along the $[11\bar{1}]$ zone axis. As shown in Fig. 3(b–d), all of the different zone axes show lattice plane spacings of 0.205 ± 0.002 nm and 0.331 ± 0.01 nm for the planes parallel and perpendicular to the long axis of the NW, respectively. All of the SAED patterns in the insets in Fig. 3(a–d) can be assigned to the tetragonal CIGS structure. The CIGS NW is clearly single crystalline in nature, with a <110> growth direction and no twins or defects.

Fig. 4 shows a cross-sectional TEM micrograph along the length of a horizontally grown CIGS NW. As can be seen in Fig. 4(a) and (b), there are clear, step-like edges on the NW. These step-like edges are formed by atomic diffusion in the horizontal direction and are the result of anisotropic growth, with the magnitude of the deposition flux determining the dominant material-flux direction towards the seed.[13]

The epitaxial relationship between the CIGS NW and the *r*-cut Al_2O_3 substrate was analysed through HR-TEM and SAED measurements, as shown in Fig. 4(c–f). The lattice distance of the planes parallel to the growth direction is 2.08 Å,

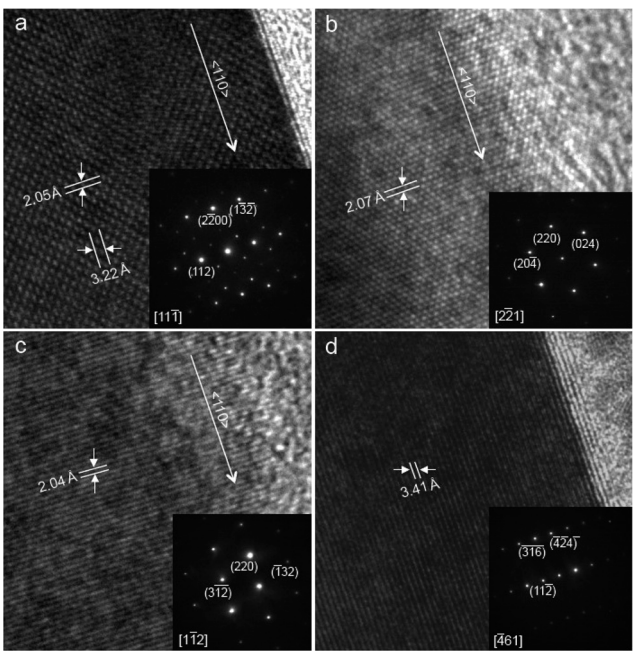

Fig. 3 The HR-TEM micrographs (a–d) and their corresponding SAED patterns (insets) at various zone axes.

 This journal is © The Royal Society of Chemistry 2015

Published on 26 May 2015. Downloaded by Korea Institute of Science and Technology / KIST on 16/06/2015 03:42:25.

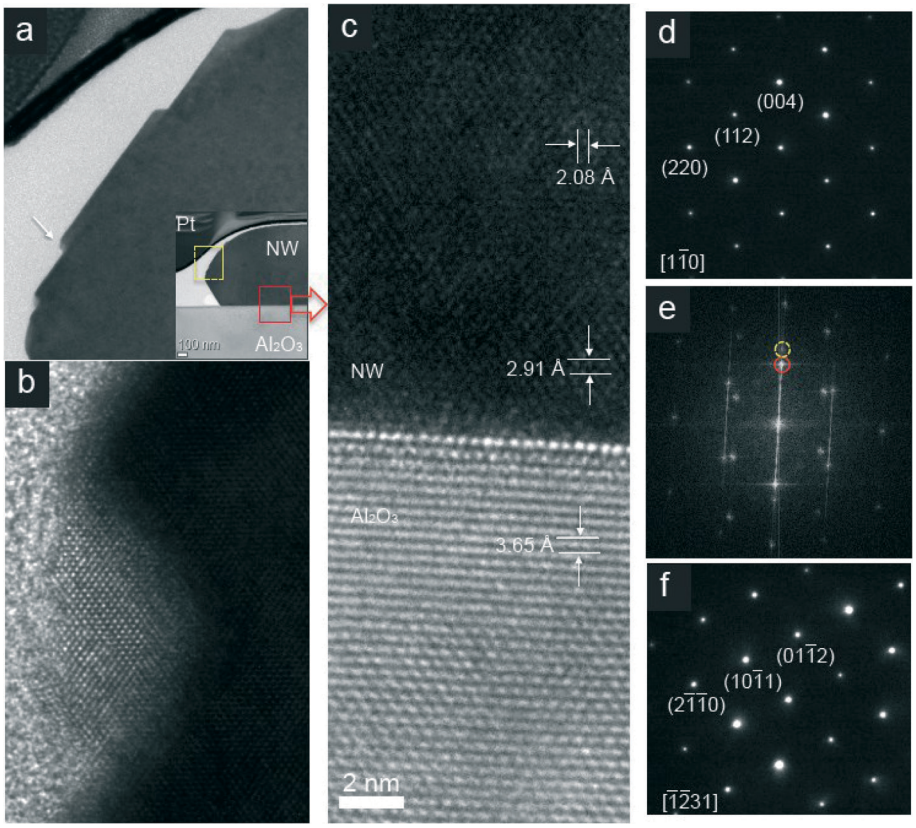

Fig. 4 (a) A cross-sectional TEM micrograph along the length of a horizontally grown CIGS NW, the region of which is marked with the dashed yellow box in the inset. The inset shows the low-magnification TEM micrograph. (b) A HR-TEM micrograph of the step edge at the tip; the position is indicated by the white arrow in Fig. 3(a). (c) A HR-TEM micrograph showing clear lattice fringes between the CIGS NW and the substrate. The corresponding SAED patterns of the (d) CIGS NW and the (f) substrate are also shown. (e) The fast Fourier transform (FFT) of the HR-TEM micrograph of the interface region is shown for epitaxial relationship analysis. The dotted yellow circle and red circle are the $(004)_{NW}$ and $(01\bar{1}2)_{substrate}$ peaks, respectively.

which corresponds well with the inter-planar spacing of the (220) planes of the CIGS chalcopyrite structure. The *d*-spacings of the (004) planes in the CIGS NW and (01$\bar{1}$2) plane of the *r*-cut Al_2O_3 substrate are 2.91 Å and 3.65 Å, respectively. The (004) planes of the horizontal CIGS NWs were aligned parallel to the (01$\bar{1}$2) plane of the Al_2O_3 substrate. Thus, the epitaxial relationship between the horizontal CIGS NWs and the *r*-cut Al_2O_3 substrate is $(004)_{NW}||(01\bar{1}2)_{substrate}$. When the (004) plane of a NW is parallel to the (01$\bar{1}$2) plane of the Al_2O_3 substrate, the CIGS NWs grow horizontally. We also evaluated the epitaxial relationship between the CIGS NWs along the radial direction and the substrate, as shown in Fig. S4.† The CIGS NWs have (112) facets, except for the (004) bottom and top surfaces. The angle between the substrate and the side plane of the NWs is 54°, which is consistent with the angle between the (004) bottom plane and the (112) side planes of the truncated triangular cross section.

We investigated the long-range lattice-matching relationship between the (004) plane of the CIGS NWs and the (01$\bar{1}$2) plane of the Al_2O_3, as shown in Fig. S5.† The [110] zone axis of the CIGS NW is parallel to the [21$\bar{3}$0] zone axis of the Al_2O_3 substrate. In addition, the lattice mismatch between the [110] direction of the CIGS NW and the [21$\bar{3}$0] direction of the *r*-cut Al_2O_3 substrate is approximately 1.5%, as shown in Fig. S5.† This indicates that CIGS NWs with a <110> growth direction are preferentially grown with the (112) side facets, which have low-index crystallographic planes and low-energy surfaces, on the basal, *r*-cut Al_2O_3 substrates. This is strong evidence for the epitaxial growth associated with a lattice mismatch between CIGS NWs and the substrate.

Other groups have tried to synthesize chalcopyrite NWs by catalyst-based methods.[6,9,10] It has been reported that CIS NWs synthesized by the vapour–liquid–solid (VLS) and solution–liquid–solid (SLS) methods grow along the [1$\bar{1}$0] and [112] directions, respectively.[9,10] It was suggested that the NWs grow in different directions because of the different synthesis methods used. For example, VLS-based NW growth is strongly affected by the catalytic reactions, while SLS-based growth is highly influenced by the ligands. We have found that the atomic structure of the substrate determines the geometry and orientation of the self-seeds, as well as the formation of low-energy crystal planes, which in turn directs the growth patterns of the CIGS NWs. We suggest that lattice mismatching is one of the most critical factors for growing NWs. To investigate the physical properties of the grown

Published on 26 May 2015. Downloaded by Korea Institute of Science and Technology / KIST on 16/06/2015 03:42:25.

NWs, we performed micro-Raman spectroscopy and PL measurements.

Fig. 5(a) shows a typical Raman spectrum of the CIGS NWs. In keeping with the selection rules for Raman scattering in CIGS materials, only the A_1 and B_2/E modes are present.

The peak position and line shape of the A_1 mode, which represents the vibration of Se anions in the x–y plane with cations at the end, are dependent on the chemical composition and crystallinity of the NWs, respectively. The B_2/E modes represent the in-phase vibrations of the anions and the cations. To determine the lateral distributions of these phases with precision, we scanned a 9×7 μm^2 area of a CIGS NW and recorded a full Raman spectrum at each position. According to the relationship between the Raman spectra and locally developed stresses, the increase in peak frequency corresponds to the compressive stress in a sample. The frequency of the A_1 mode increases as the Cu/(In + Ga) content ratio decreases, *e.g.*, shifting the peak from 173 cm^{-1} (Cu/(In + Ga) = 1.17) to 176 cm^{-1} (Cu/(In + Ga) = 0.78). It also increases as the Ga/(In + Ga) content ratio increases, *e.g.*, shifting from 173 cm^{-1} (for CIS) to 181 cm^{-1} (for $CuGaSe_2$).[16–19] As shown in Fig. 4(a), the frequency of the chalcopyrite A_1 mode for the CIGS NW with content ratios of Ga/(In + Ga) = 0.8 and Cu/(In + Ga) = 0.9 is approximately 178 cm^{-1}. This value is higher than that of CIS thin films (173 cm^{-1}), which indicates lattice compression because the Ga content of the CIGS NWs is significantly higher than that of the thin films. The A_1 mode, which has a sharp, line-like shape and is marked with a red dotted box in Fig. 5(a), reflects the high crystallinity of the CIGS NWs, which were uniformly grown, as shown in the bright image in Fig. 5(b). The bright areas signify regions of high Raman intensity in the frequency region of an individual mode. The dark areas represent regions without an individual mode. The two peaks corresponding to the B_2/E modes are also present at 218 cm^{-1} and 254 cm^{-1}, respectively, and are indicated with a blue dotted box. As can be seen in Fig. 5(c), their modes are absent from the middle region of the NW. Based on the results of the Raman analysis, we have confirmed that the CIGS NWs grown on the r-cut Al_2O_3 substrate have a chalcopyrite structure, are Ga rich, and have a high crystallinity.

Fig. 6(a) shows the micro-PL spectrum of a CIGS NW that was measured at 10 K and an excitation power intensity of 100 mW; the spectrum is similar to the typical PL spectrum of a CIGS thin film. The CIGS NW exhibits a dominant near-band-edge (NBE) PL peak at 1.12 eV, which could be attributed to a donor–acceptor pair (DAP) transition.[20] The PL peak at 0.98 eV is attributed to defect-related free-to-bound (F–B) transitions. Thus, the defect level is approximately 140 meV and too deep for an isolated copper vacancy (V_{Cu}). However, it may be related to a defect complex that includes V_{Cu}. To determine whether the PL peaks were related to F–B or DAP transitions, the temperature dependence of the peak energy was investigated. Fig. 6(b) shows the temperature dependence of the macro-PL spectrum of the CIGS NWs.

A DAP transition at 1.12 eV is the dominant peak in the PL spectrum of the CIGS NWs. As the temperature increases, the PL intensity of the DAP decreases until it is completely absent at temperatures above 150 K. The PL peak at 1.12 eV is attributed to a DAP transition because a distant DAP transition with a long radiative lifetime becomes ionized at higher temperatures. To confirm the origin of the peaks, the dependence of the PL spectrum on the excitation intensity was measured. The blue shift of the PL energy as a function of the excitation power is a well-known phenomenon in the case of DAP transitions.[21] Fig. 6(c) shows the low-temperature macro-PL spectra (measured at 12 K) of the CIGS NWs at various excitation intensities. As can be seen in Fig. 6(d), at 12 K, the DAP peak exhibits a blue shift of 10 meV as the excitation intensity increases. This asymmetric PL peak has a steep high-energy slope and a gentle low-energy slope under high excitation intensities, but these slopes are reversed under low excitation intensities. This change in the PL line shape with the applied excitation intensity is a characteristic of broad DAP peaks.[22,23] Thus, the CIGS NWs with high Ga contents have a bandgap of 1.12 eV. As a result, it may be possible to enhance solar cells with the application of

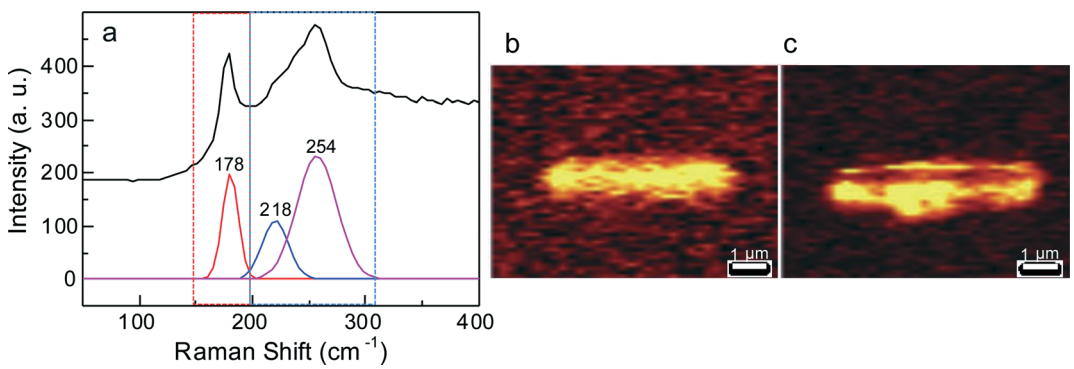

Fig. 5 (a) A typical Raman spectrum of a horizontal CIGS NW recorded at room temperature. The black line in the upper part of the figure is the Raman spectrum. The original Raman spectrum is fitted to the red line of the A_1 mode at 178 cm^{-1}, and the blue and pink lines at 218 cm^{-1} and 254 cm^{-1} of the B_2/E modes, respectively. (b) and (c) are high-resolution Raman images of the A_1 mode, as indicated by the red dotted box, and the B_2/E mode, as indicated by the blue dotted box in Fig. 5(a), respectively. These images show the integral intensities of the Raman modes.

 This journal is © The Royal Society of Chemistry 2015

Published on 26 May 2015. Downloaded by Korea Institute of Science and Technology / KIST on 16/06/2015 03:42:25.

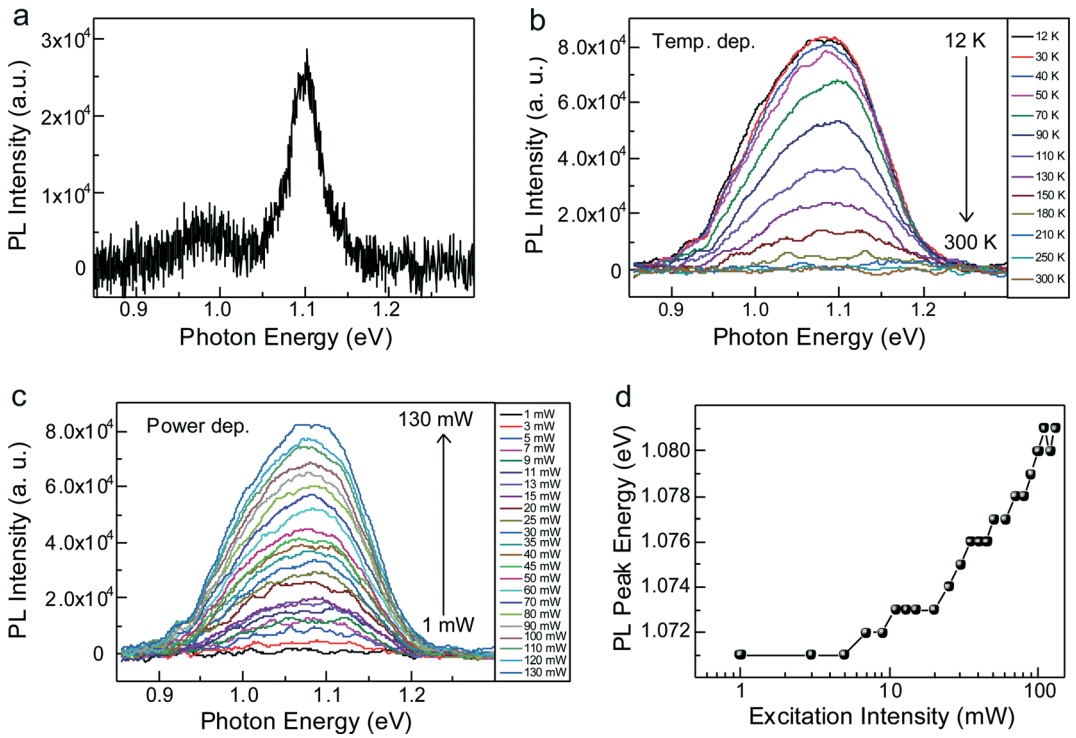

Fig. 6 (a) A micro-PL spectrum of a horizontal CIGS NW, which was recorded at approximately 10 K. (b) Temperature dependence of the macro-PL spectrum. The excitation energy was fixed at 130 mW. (c) Excitation power intensity dependence of the macro-PL spectrum. These measurements were performed at 12 K. (d) Excitation power intensity dependence of the peak position.

single-crystal CIGS NWs with a uniform composition and a high absorption coefficient. Furthermore, it should be possible to produce new device architectures that make use of CIGS NWs in photodetectors and photovoltaic systems.

Conclusions

In conclusion, we synthesized epitaxially grown single-crystal CIGS NWs with a vapour-phase transport process that does not require any catalysts. We were able to control the growth mode of the single-crystal CIGS NWs by adjusting the gas deposition flux of the evaporated sources with a specially designed alumina boat. The freestanding CIGS NWs ranged approximately 50–700 nm in diameter and 1–20 μm in length, while the horizontally grown CIGS NWs ranged approximately 500–1500 nm in diameter and 1–100 μm in length. The Cu/(In + Ga) ratios of the freestanding and horizontally grown CIGS NWs were 1.1 and 0.9, respectively, while their Ga/(In + Ga) ratios were 0.78 and 0.81, respectively. Each constituent element in the CIGS NWs was uniformly distributed along the growth direction of the NWs. CIGS NWs with a <110> growth direction were preferentially grown with the (112) side facets, which have low-index crystallographic planes and low-energy surfaces, on the *r*-cut Al_2O_3 substrate. The bandgap energy of the CIGS NWs with a high Ga content was 1.12 eV. We believe that the single-crystal CIGS NWs are suitable for manufacturing new devices and can be fabricated by controlling the carrier mobilities of their constituent elements. These CIGS NWs could be used in a wide range of nanodevice-based applications, such as photodetectors and photovoltaic systems.

Acknowledgements

We acknowledge the financial support through grants from the internal projects of KIST, the National Research Foundation of Korea (NRF) (no. 20110030803 and 20110019984), and the Center for Advanced Meta-Materials (CAMM no. 2014063701, 2014063700), which were funded by the Ministry of Science, ICT, and Future Planning. Financial support was also provided by the Ministry of Knowledge Economy (MKE, Korea) through the Industrial Strategic Technology Development Program (grant no. 10041589).

References

1 S. Wagner, J. Shay, P. Migliorato and H. Hasper, *Appl. Phys. Lett.*, 1974, **25**, 434–435.
2 H. W. Schock and R. Noufi, *Prog. Photovoltaics*, 2000, **8**, 151–160.
3 P. Jackson, D. Hariskos, E. Lotter, S. Paetel, R. Wuerz, R. Mener, W. Wischmann and M. Powalla, *Prog. Photovoltaics*, 2011, **19**, 894–897.
4 Q. Cao, O. Gunawan, M. Copel, K. B. Reuter, S. J. Chey, V. R. Deline and D. B. Mitzi, *Adv. Energy Mater.*, 2011, **1**, 845–853.
5 A. Chirila, S. Buecheler, F. Pianzzi, P. Bloesch, C. Gretener, A. R. Uhl, C. Fella, L. Kranz, J. Perrenoud, S. Seyrling, R.

Published on 26 May 2015. Downloaded by Korea Institute of Science and Technology / KIST on 16/06/2015 03:42:25.

Verma, S. Nishiwaki, Y. E. Romanyuk, G. Bilger and A. N. Tiwari, *Nat. Mater.*, 2011, **10**, 857–861.
6 J. Tang, Z. Huo, S. Brittman, H. Gao and P. Yang, *Nat. Nanotechnol.*, 2011, **6**, 568–572.
7 Y. H. A. Wang, X. Zhang, N. Bao, B. Lin and A. Gupta, *J. Am. Chem. Soc.*, 2011, **133**, 11072–11075.
8 R. Inguanta, P. Livreri, S. Piazza and C. Sunseri, *Electrochem. Solid-State Lett.*, 2010, **13**, K22–K25.
9 H. Peng, D. T. Schoen, S. Meister, X. F. Zhang and Y. Cui, *J. Am. Chem. Soc.*, 2007, **129**, 34–35.
10 A. J. Wooten, D. J. Werder, D. J. Williams, J. L. Casson and J. A. Hollingsworth, *J. Am. Chem. Soc.*, 2009, **131**, 16177–16188.
11 M. G. Panthani, V. Akhavan, B. Goodfellow, J. P. Schmidtke, L. Dunn, A. Dodabalapur, P. F. Barbara and B. A. Korgel, *J. Am. Chem. Soc.*, 2008, **130**, 16770–16777.
12 J. Xu, C. Y. Luan, Y. B. Tang, X. Chen, J. A. Zapien, W. J. Zhang, H. L. Kwong, X. M. Meng, S. T. Lee and C. S. Lee, *ACS Nano*, 2010, **4**, 6064–6070.
13 Y. D. Yoo, K. Y. Seo, S. Han, K. S. K. Varadwaj, H. Y. Kim, J. H. Ryu, H. M. Lee, J. P. Ahn, H. T. Ihee and B. S. Kim, *Nano Lett.*, 2010, **10**, 432–438.
14 W. K. Seong, J. Y. Huh, W. N. Kang, J. W. Kim, Y. S. Kwon and N. K. Yang, *Chem. Vap. Deposition*, 2007, **13**, 680–683.
15 J. E. Jaffe and A. Zunger, *Phys. Rev. B: Condens. Matter Mater. Phys.*, 2001, **64**, 241304.
16 A. R. Jeong, W. Jo, M. Song and S. Yoon, *Mater. Chem. Phys.*, 2012, **134**, 1030–1035.
17 W. Witte, R. Kniese and M. Powalla, *Thin Solid Films*, 2008, **517**, 867–869.
18 M. G. Park, S. J. Ahn, J. H. Yun, J. H. Gwak, A. Cho, S. K. Ahn, K. S. Shin, D. H. Nam, H. S. Cheong and K. H. Yoon, *J. Alloys Compd.*, 2012, **513**, 68–74.
19 I. H. Choi, *Thin Solid Films*, 2011, **519**, 4390–4393.
20 S. Shirakata, K. Ohkubo, Y. Ishii and T. Nakada, *Sol. Energy Mater. Sol. Cells*, 2009, **93**, 988–992.
21 Y. Chiba, A. Yamada, M. Konagai, Y. Matsuo and T. Wada, *Jpn. J. Appl. Phys.*, 2008, **47**, 694–696.
22 S. B. Zhang, S.-H. Wei, A. Zunger and H. Katayama-Yoshida, *Phys. Rev. B: Condens. Matter Mater. Phys.*, 1998, **57**, 9642–9656.
23 E. Zacks and A. Halperin, *Phys. Rev. B: Solid State*, 1972, **6**, 3072–3075.

 This journal is © The Royal Society of Chemistry 2015